DTU Library

Effects of ambient pressure and nozzle diameter on ignition characteristics in diesel spray combustion

Ong, Jiun Cai; Walther, Jens Honore; Xu, Shijie; Zhong, Shenghui; Bai, Xue-Song; Pang, Kar Mun

Link back to DTU Orbit

Effects of ambient pressure and nozzle diameter on ignition characteristics in diesel spray combustion

Jiun Cai Ong[a,*], Jens Honore Walther[a,b], Shijie Xu[c], Shenghui Zhong[c,d],
Xue-Song Bai[c], Kar Mun Pang[e]

[a]*Department of Mechanical Engineering, Technical University of Denmark, Nils Koppels
Allé, 2800 Kgs, Lyngby, Denmark*
[b]*Computational Science and Engineering Laboratory, ETH Zürich, Clausiusstrasse 33,
Zürich CH-8092, Switzerland*
[c]*Department of Energy Sciences, Lund University, 22100 Lund, Sweden*
[d]*State Key Laboratory of Engines, Tianjin University, 135 Yaguan Rd, Tianjin 300350,
China*
[e]*MAN Energy Solutions, Teglholmsgade 41, 2450 København SV, Denmark*

Abstract

Numerical simulations are performed to investigate the effects of ambient density
(ρ_{am}) and nozzle diameter (D_{noz}) on the ignition characteristic of diesel spray
combustion under engine-like conditions. A total of nine cases which consist of
different ρ_{am} of 14.8, 30.0, and 58.5 kg/m^3 and different D_{noz} of 100, 180, and
363 μm are considered. The results show that the predicted ignition delay times
are in good agreement with measurements. The current results show that the
mixture at the spray central region becomes more fuel-rich as D_{noz} increases.
This leads to a shift in the high-temperature ignition location from the spray tip
towards the spray periphery as D_{noz} increases at ρ_{am} of 14.8 kg/m^3. At higher
ρ_{am} of 30.0 and 58.5 kg/m^3, the ignition locations for all D_{noz} cases occur
at the spray periphery due to shorter ignition timing and the overly fuel-rich
spray central region. The numerical results show that the first ignition location
during the high-temperature ignition occurs at the fuel-rich region at $\rho_{\mathrm{am}} \leqslant$
30.0 kg/m^3 across different D_{noz}. At $\rho_{\mathrm{am}} = 58.5$ kg/m^3, the ignition occurs at
the fuel-lean region for the 100 and 180 μm cases, but at the fuel-rich region for
the 363 μm nozzle case. This distinctive difference in the result at 58.5 kg/m^3 is

---

[*]Corresponding author
   Email address: `jcong@mek.dtu.dk` (Jiun Cai Ong)

likely due to the relatively longer ignition delay time in the $363\,\mu$m nozzle case. Furthermore, the longer ignition delay time as D_{noz} increases can be related to the higher local scalar dissipation rate in the large nozzle case.

Keywords: Spray flame, Transported probability density function, Ignition process, Ambient density effect, Nozzle diameter effect

1. Introduction

Automotive and marine industries have worked to improve the understanding of in-cylinder processes in order to design engines that are cleaner and more efficient. Sandia National Laboratory and numerous research groups have shared their optical measurements and numerical modeling results through the Engine Combustion Network (ECN) [1] to facilitate the study of diesel spray combustion and for validation of numerical model. Effects of a wide range of diesel engine parameters on fuel penetration, ignition delay time (IDT), flame lift-off length (LOL), and soot emissions have been studied [2, 3, 4]. Extensive and comprehensive studies have been carried out for Spray A configuration, where the ambient gas density (ρ_{am}) and nozzle diameter size (D_{noz}) are set to $22.8\,\text{kg/m}^3$ and $90\,\mu$m, respectively. The ambient temperature (T_{am}) is set to $900\,\text{K}$, while its corresponding ambient pressure (P_{am}) is $58\,\text{bar}$. Significant emphasis has been placed on understanding its ignition and flame stabilization processes [5, 6, 7, 8]. It was only recently that ECN introduced the Spray D configuration [9, 10], which has the same operating conditions as Spray A, but uses a larger nozzle diameter, $D_{\text{noz}} = 186\,\mu$m. Different ignition characteristics were observed in Spray D than that in Spray A at $900\,\text{K}$, where ignition was shown to occur at the spray periphery in the former case [10] instead of occurring at the spray head for the latter case. The results suggest that the favorable ignition location shifts to the peripheral of the spray as nozzle diameter increases.

It is important to note that most of the aforementioned studies were performed at ambient density, $\rho_{\text{am}} = 14.8 - 30.0\,\text{kg/m}^3$. However, the ρ_{am} at the start of injection is approximately $60.0\,\text{kg/m}^3$ under full load conditions in typical

2

heavy-duty engines and large two-stroke marine engines. Meanwhile, the D_{noz} in marine engines are generally larger in order to deliver a greater amount of fuel. For instance, the fuel injector in the medium-speed four-stroke marine engines simulated by Kyriakides et al. [11] and Kilpinen [12] had a size of 370 μm and 388 μm, respectively. Ishibashi and Tsuru [13] performed multiple injection experiments under marine engine-like conditions, in which the pilot diesel injector and main diesel injector had a size of 160 μm and 500 μm, respectively. Schmid et al. [14] conducted experiments using an optical accessible marine spray combustion chamber with swirling flow, in which the fuel is injected from a 875 μm nozzle. Bolla et al. [15] later used the same experimental setup to study a range of D_{noz} from 200 to 1200 μm. However, it is important to note that the experiment is only conducted at a constant density of 33 kg/m^3. Experimental studies of spray combustion conducted in a constant volume chamber under high ρ_{am} (or P_{am}) and large D_{noz} were reported by Siebers and co-workers [3, 16, 17, 18, 19]. The experimental studies were carried out for a range of ρ_{am} from 7.3 to 58.5 kg/m^3, which corresponds to P_{am} of 20 to 170 bar when T_{am} is at 1000 K. Both liquid and vapor penetration lengths were found to decrease with increasing ρ_{am}. Meanwhile, spray flame at quasi-steady state were found to reduce in size (both in length and width) when ρ_{am} increases [3, 18]. In terms of ignition and premixed combustion processes, Higgins et al. [19] investigated them up to 45.0 kg/m^3 but only for D_{noz} of 246 μm. Their work showed that increasing density decreases the time for ignition to occur. In addition, the ignition location was shown to move around the central region of the spray containing liquid-phase fuel and extend upstream along its sides.

From a simulation point of view, Cung et al. [20] performed Unsteady Reynolds Averaged Navier-Stokes (URANS) simulations to study the influence of nozzle diameter on spray combustion and soot emissions in Spray A conditions. The SAGE detailed chemistry solver [21], which is a well-mixed reactor based model was used in the study. The tested nozzle diameters ranged from 30 to 129 μm. They noticed that the IDT varies non-linearly with nozzle diameter where the shortest ignition delay occurs for the 70 μm nozzle case. Nozzles with

3

smaller diameter delayed the ignition due to leaner mixture (less injected fuel mass and high levels of air entrainment) at ignition sites [20]. As the nozzle diameter decreased, the equivalence ratio contour line shifted toward leaner mixtures at the same axis location. Comparison of Spray A and Spray D was carried out in the numerical study by Desantes et al. [22]. The unsteady flamelet progress variable (UFPV) model was employed in the study. It was shown that a reduction in D_{noz} promotes faster mixing which shortens the time needed to reach ignitable equivalence ratio, therefore a shorter IDT was observed in the Spray A case. In addition, Ong et al. [23] compared the ignition characteristics between Spray A and Spray D by performing large eddy simulations coupled with partially-stirred reactor model. Their simulations were able to predict the annular ignition sites for Spray D at ambient temperatures of 1000 and 900 K, which is consistent with the experimental observation in [10]. It was suggested by Ong et al. [23] that the less fuel-rich mixture at the spray periphery is more favorable for ignition than the relatively more fuel-rich mixture at the core of the spray in Spray D. Pang et al. [24] performed a URANS study on reacting sprays in a constant volume combustion vessel with D_{noz} of 100, 180, and 363 μm. Their numerical results showed that as D_{noz} becomes larger, the low-temperature region of the spray tends to get more fuel-rich. Their simulation was able to capture the spray flame feature across different D_{noz}, in particular the flame penetration length. However, little focus was placed on the ignition characteristic of different D_{noz}.

All the numerical works mentioned above for different D_{noz} were only performed at a single ρ_{am}. On the other hand, the effects of ρ_{am} on ignition and spray flame were carried out by Pang et al. [25]. Their 3-D numerical study investigated the ignition behaviors and flame structures at different ρ_{am} of 14.8, 30.0, and 58.5 kg/m^3. They found that the mixture fraction (Z) of the first igniting location during the high-temperature ignition does not vary monotonically with ρ_{am}. The ignition occurred at a fuel-rich mixture region for the 14.8 and 30.0 kg/m^3 cases, but at a fuel-lean mixture region for the 58.5 kg/m^3 case. It is important to note that the work was carried out only for single D_{noz} of

4

87 180 μm. The coupled effects between D_noz and ρ_am on ignition characteristics

88 are still not completely understood. The variation of the ignition mixture during

89 initial high-temperature ignition with respect to ρ_am may vary as D_noz becomes

90 larger or smaller. This information is critical to the development of skeletal

91 surrogate fuel mechanisms. Developing a mechanism that fits into a narrower

92 range of operating conditions would allow the size of the fuel mechanisms to be

93 further optimized, thus increasing computational efficiency.

94 Set against these backgrounds, the objective of the present CFD work is to

95 investigate the effects of varying D_noz and ρ_am on the ignition process in diesel

96 spray flame. The velocity, species, and temperature distribution profiles are

97 computed and compared to elucidate the differences in the ignition process. The

98 paper is structured such that experimental data used for model validation are

99 first described in Section 2. Next is the descriptions of the numerical methods in

100 Section 3. Sections 4 and 5 present the model validation as well as the numerical

101 analysis of autoignition at different ρ_am and D_noz. Conclusions from this work

102 are highlighted in the final section.

103 2. Case descriptions

104 The grade number two Diesel fuel (Diesel #2) spray experimental data

105 [1, 17, 18] obtained from constant volume spray combustion experiment is

106 used for model validation in this work. The constant volume chamber has

107 an ambient gas composition of 21.0 % O_2, 69.3 % N_2, 6.1 % CO_2 and 3.6 % H_2O

108 (by volume) before the start of spray injection. This experimental ambient gas

109 composition is used in the current reacting spray cases to ensure identical initial

110 thermochemical conditions.

111 As depicted in Table 1, reacting spray simulations are carried out for three

112 D_noz of 100, 180, and 363 μm. Three ρ_am of 14.8, 30.0, and 58.5 $\mathrm{kg/m^3}$ are

113 considered for each D_noz. At $T_\mathrm{am} = 1000\,\mathrm{K}$, the ρ_am considered corresponds to

114 P_am of 42, 85, and 170 bar, respectively. Initial flow and turbulence conditions

115 can be found in the previous work [26]. The operating conditions and the

5

Table 1: Operating conditions and injection specifications.

Case	O_2 [% mol]	T_{am} [K]	ρ_{am} [kg/m^3]	D_{noz} [μm]	P_{inj} [bar]	$\dot{m}_f$ [g/s]
1	21	1000	14.8	100	1400	2.7
2	21	1000	30.0	100	1400	2.8
3*	21	1000	58.5	100	1400	2.8
4	21	1000	14.8	180	1400	8.8
5	21	1000	30.0	180	1400	9.0
6	21	1000	58.5	180	1400	9.2
7	21	1000	14.8	363	1400	35.8
8	21	1000	30.0	363	1400	36.3
9*	21	1000	58.5	363	1400	36.3

*No experimental injected fuel mass flow rate ($\dot{m}_f$) is available for $\rho_{am} = 58.5$ kg/m^3. The $\dot{m}_f$ for $\rho_{am} = 30.0$ kg/m^3 case is used instead.

injection specifications, such as D_{noz}, injection pressure (P_{inj}), and injected fuel mass flow rate ($\dot{m}_f$), for each test cases are listed in Table 1.

3. CFD model formulation

The 3-D CFD spray combustion simulations are carried out using OpenFOAM-v1712. The fuel spray, flow and combustion processes are modeled using the Eulerian-Lagrangian approach within the URANS framework. Realizable k–ϵ model [27] is employed for turbulence modeling. The injected liquid phase of the fuel is modeled as discrete parcels whose motion is described using the Lagrangian particle tracking approach. Each parcel represents a group of spherical droplets whose position, size, and physical properties are similar. Primary breakup of the injected fuel is considered by injecting computational parcels with the Rosin-Rammler distribution of diameter ranging from $0.1D_{noz}$ to D_{noz}. The secondary breakup is modeled by the Reitz-Diwakar spray model

[28]. As each nozzle has its own nozzle coefficients (available in [1]), the stripping breakup constant, C_s, in the Reitz-Diwakar model for the nozzle cases of 100, 180, and 363 μm are set to 13, 6, and 8, respectively. It is important to note that for each D_noz case the same C_s value is used across the three ρ_am tested. The liquid properties of tetradecane ($C_{14}H_{30}$) are used to represent Diesel #2 fuel [29]. The Frossling model and the Ranz-Marshall correlation are employed to account for the droplet evaporation and heat transfer with the surrounding gas phase respectively.

The turbulence-chemistry interaction (TCI) is modeled using an Eulerian-based transported probability density function (PDF) method, the Eulerian Stochastic Field (ESF) method [30]. Similar to the Lagrangian particle transported PDF method, the ESF method is a general approach to account for TCI effect. It can be used to simulate the autoignition as well as different levels of "premixedness", *i.e.*, premixed, partially premixed and non-premixed. Details of the ESF formulation are available in [30]. The model has been applied successfully to simulate diesel spray combustion [24, 25, 31, 32]. The number of stochastic fields is set to 32 as the result was shown to have reached convergence [32]. The Chemistry Coordinate Mapping (CCM) approach is coupled with the ESF solver to speed up the integration process of the chemical reaction rates [33]. The current work uses a four-dimensional phase space based on temperature, local equivalence ratio, scalar dissipation rate, and the mass fraction of fuel, where the resolutions of CCM are fixed at 5K, 0.01, 0.025, and 0.001, respectively [32, 33].

The computational domain is a constant volume cubic chamber with side lengths of 108 mm, which corresponds to the volume of the experimental combustion vessel [1]. The ambient mixture composition, pressure, and temperature are initiated as uniform field while the velocity field is set to zero. All boundaries are set as no-slip wall with Neumann boundary condition for the ambient mixture composition, pressure, and temperature. The injector is placed at the center of one of the chamber walls. The mesh configuration used in [25] is employed in the present study which involves an isotropic cell size of 0.5 mm within the spray combustion region. This mesh configuration was shown to reach mesh

7

independence in [25].

4. Model Validation

4.1. Inert spray validation

Model evaluation is performed on evaporating sprays (Cases 1-9 shown in Table 1) at different ρ_{am} and D_{noz} values by computing the liquid penetration length (LPL) and vapor penetration length (VPL). This is first carried out by performing inert spray simulations where O_2 is set to zero. LPL is defined as the maximum axial location from the injector to the location where 95 % of the total liquid mass is found; VPL is determined using the farthest downstream location of 0.1 % fuel mass fraction.

Since experimental data are not available, model evaluation of the liquid-phase is carried out by comparing against the LPL obtained from the liquid scaling law [16]. The liquid properties of n-heptadecane are used in the liquid scaling law to produce Diesel #2 liquid length [16] since these resemble the properties of Diesel #2. Figure 1 shows the computed LPL and VPL for different D_{noz} at different ρ_{am} of 14.8, 30.0, and 58.5 kg/m^3. In the figure, the computed LPL are shown to be comparable to the LPL obtained from the liquid scaling law across different ρ_{am}.

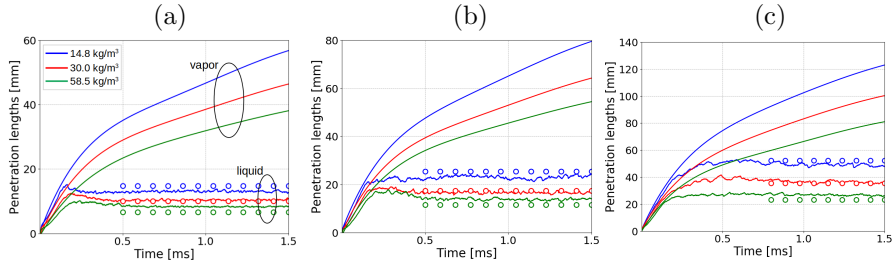
Figure 1: Liquid and vapor penetration lengths of the non-reacting sprays as a function of time after start of injection (ASI) for different D_{noz} of (a) 100, (b) 180, and (c) 363 μm. Solid lines denote the simulations results. Circle markers denote the liquid scaling law results [16].

On the other hand, the associated VPLs shown in Figure 1 are evaluated using the dimensionless penetration length, σ and dimensionless penetration
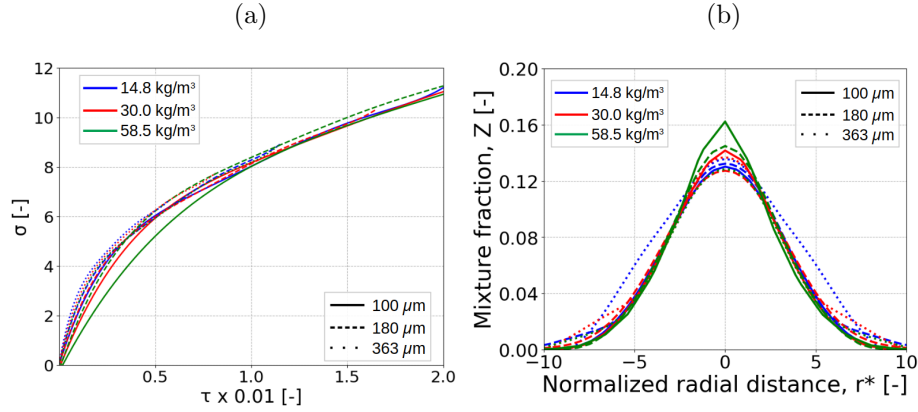
(a)   (b)

Figure 2: (a) Dimensionless penetration length (σ) as a function of dimensionless penetration time (τ) and (b) mixture fraction distribution along normalized radial direction, r^* at normalized axial distance, $x^* = 40$ for different ρ_{am} of 14.8, 30.0, and 58.5 kg/m^3. Solid-, dashed- and dotted-lines are results for D_{noz} of 100, 180, and 363 μm, respectively.

time, τ. Detailed methodology to calculate σ and τ can be found in [17]. As seen in Figure 2a, all the σ curves collapse on to one another, which agrees with the trend reported in [17]. This indicates that the dependence of VPL on D_{noz} and ρ_{am} is successfully simulated by the model.

It is shown in [10, 22] that the profiles of mixture fraction for two different D_{noz} collapse onto one another in normalized coordinates. Therefore, similar methodology from [10, 22] is applied to analyze the profiles of mixture fraction for Cases 1–9 (in Table 1. Figure 2b shows the mixture fraction (Z) fields from cases with varying ρ_{am} and D_{noz} (Cases 1–9) compared together in normalized radial (r^*) and axial (x^*) coordinates. The normalized coordinates r^* and x^* are computed by normalizing the radial (r) and axial coordinate (x) by the equivalent diameter (d_{eq}) of each nozzle, i.e., $r^* = r/d_{eq}$ and $x^* = x/d_{eq}$ [10, 22]. The equivalent diameter is calculated as $d_{eq} = D_{noz}\sqrt{\rho_f/\rho_{am}}$, where ρ_f denotes the density of the fuel. It is shown in Figure 2b that the mixture fraction profiles from different ρ_{am} and D_{noz} collapse onto one another. This implies that the dependence of mixture fraction distribution on ρ_{am} and D_{noz} is also successfully simulated by the model.

9

4.2. Reacting Spray Validation

Two n-heptane (C_7H_{16}) mechanisms are evaluated in this section. The two mechanisms are the reduced C_7H_{16} mechanism (68 species and 283 reactions) developed by Lu et al. [34], and the mechanism (44 species and 112 reactions) developed by Liu et al. [35]. The mechanisms are henceforth denoted as Lu68 and Liu44, respectively. These two mechanisms have shown good performance in spray combustion context [24, 32, 25, 36]. The IDTs predicted by the two mechanisms for different D_{noz} and ρ_{am} are simulated and compared against measurement data [1], as shown in Figure 3. The IDT is defined as the time taken for the mixture temperature to increase by 400 K from its initial temperature ($\Delta T = 400\,K$), following the definition in [25]. The IDT predicted by Liu44 overpredicts the IDT by 27 % in the low density case ($14.8\,kg/m^3$), but underpredicts by 37 % in the high density case ($58.5\,kg/m^3$). Overall, the results from Lu68 are in better agreement than those of Liu44 with the experimental data. For a fixed D_{noz}, the computed IDTs are shown in Figure 3 to decrease with increasing ρ_{am}, which correspond with measurements. At all three ρ_{am}, the simulated IDTs are shown to increase with D_{noz}. This agrees with the measurement trend at $\rho_{am} = 14.8\,kg/m^3$. However, a non-monotonic trend is observed for the measurement data at $30.0\,kg/m^3$ where the IDT increases from 100 to $180\,\mu m$, but decreases from 180 to $363\,\mu m$. This discrepancy may be due to the experimental uncertainties caused by the hydraulic delay during fuel injection [37]. Despite this, the relative errors across different ρ_{am} and D_{noz} are less than 50 % for the Lu68 mechanism. In addition to this, the performance of the Lu68 mechanism in a zero-dimensional homogeneous reactor is available in the Appendix A1.

5. Results & Discussion

In this section, the autoignition characteristics for different D_{noz} at ρ_{am} of $14.8\,kg/m^3$ (Figure 4), $30.0\,kg/m^3$ (Figure 6), and $58.5\,kg/m^3$ (Figure 8) are studied using scatter plots of the temperature-mixture fraction (T-Z) and
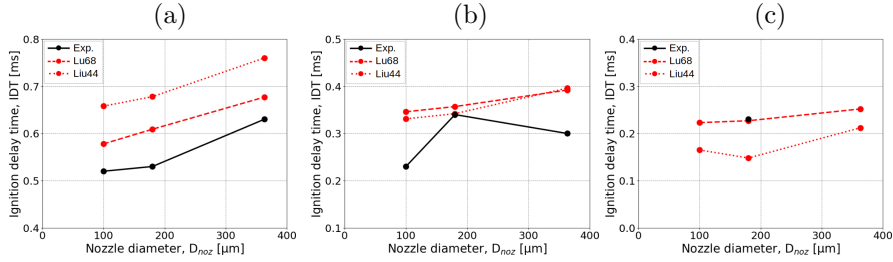
Figure 3: Ignition delay time, IDT as a function of nozzle diameter, D_{noz} at different ρ_{am} of (a) 14.8, (b) 30.0, and (c) 58.5 kg/m^3. Solid-lines denote experimental results. Dashed- and dotted-lines denote the simulation results from Lu68 and Liu44 mechanisms, respectively.

226 contours of various combustion products. For all the cases (shown in Table 1),
227 the low-temperature ignition first initiates in fuel-lean region ($Z < Z_{\mathrm{st}}$), where
228 Z_{st} is the stoichiometric mixture fraction with a value of 0.062. It is followed by
229 a temperature rise within the fuel-rich region ($Z > Z_{\mathrm{st}}$). Thereafter, the high-
230 temperature combustion occurs within a relatively less-rich mixture. These
231 observations agree with the findings by Pei et al. [38]. Despite this, there are
232 still distinct differences in the ignition characteristics as ρ_{am} and D_{noz} change,
233 which will be discussed in detail in the following sections.

234 *5.1. Ignition characteristics at $\rho_{\mathrm{am}} = 14.8\,kg/m^3$*

235   For the 100 μm case at 14.8 kg/m^3, high concentration of RO$_2$ is shown
236 to form in the fuel-rich inner core of the spray at $t = 0.540$ ms (cf. Figure 4a).
237 Through the low-temperature reaction pathway, RO$_2$ oxidizes to form ketohydro-
238 peroxide (KET) which also resides in the inner core of the spray. At this time
239 instance, HO$_2$ radicals form around the vicinity of KET where the spray region
240 is fuel-rich, as shown in Figure 4a. The T-Z diagram in Figure 4a also shows
241 the presence of OH in the fuel-rich side with a peak temperature of ~ 1100 K. It
242 is notable that RO$_2$, KET and HO$_2$ are formed downstream of the liquid fuel.
243   At $t = 0.588$ ms (Figure 4b), high concentration of HO$_2$ is seen forming at
244 two distinct regions in the spray: the L-region which has low local temperature
245 with fuel-richer mixture composition, and the H-region which has relatively
246 higher local temperature as well as less fuel-rich mixture composition. Moreover,

11

it is illustrated in Figure 4b that OH is present at the H-region, thus implying that HO_2 has been consumed and undergone high-temperature reaction to form OH. The local temperature is also shown to increase beyond the temperature threshold of $1400\,K$ ($400\,K$ above T_{am}), which indicates the onset of the main ignition.

The ignition characteristics for the 180 and $363\,\mu m$ nozzle cases are illustrated in Figures 4d-f and 4g-i, respectively. During the low-temperature ignition stage at $0.574\,ms$, HO_2 and OH are present at the fuel-rich side in the $180\,\mu m$ case (cf. Figure 4d). It is also important to note that the high-temperature ignition in all three D_{noz} cases occurs in the fuel-rich side at ρ_{am} of $14.8\,kg/m^3$.

A noticeable difference when D_{noz} increases is the low- and high-temperature ignition process occurring later in time. This is expected as the IDT is shown previously to increase with increasing D_{noz} (cf. Figure 3). The effects of D_{noz} and ρ_{am} on IDT will be further discussed in Section 5.4. Meanwhile, it is shown in Figure 4 that the onset of high-temperature ignition occurs at the spray head for D_{noz} of $100\,\mu m$, which is similarly obtained in the 3-D large eddy simulations by Irannejad et al. [39]. However, the ignition location is seen to shift to the spray periphery as D_{noz} increases to $363\,\mu m$. This can be attributed to the overly fuel-rich region in the spray central region as D_{noz} increases. Figure 5 shows the scatter plots of T, colored by different ranges of Z, along the spray axis for both the central and peripheral region of different D_{noz} at $\rho_{am} = 14.8\,kg/m^3$. The radial distance from the spray axis is denoted as R. The central region of the spray is defined as the region where $R \leqslant d_{eq}$, while the peripheral region is defined as $R > d_{eq}$. Onset of high-temperature ignition is observed at both the spray center and periphery for the $100\,\mu m$ case, as depicted in Figure 5a. However, as D_{noz} increases to $180\,\mu m$ and $363\,\mu m$, the onset of high-temperature ignition is shown to occur at the spray periphery (cf. Figures 5b and c), where the temperature rise in spray central region of the latter case is significantly lower than in the spray periphery.

Moreover, the evaporative cooling of the injected liquid fuel reduces the temperature of the mixtures at the inner spray region near the LPL, as compared
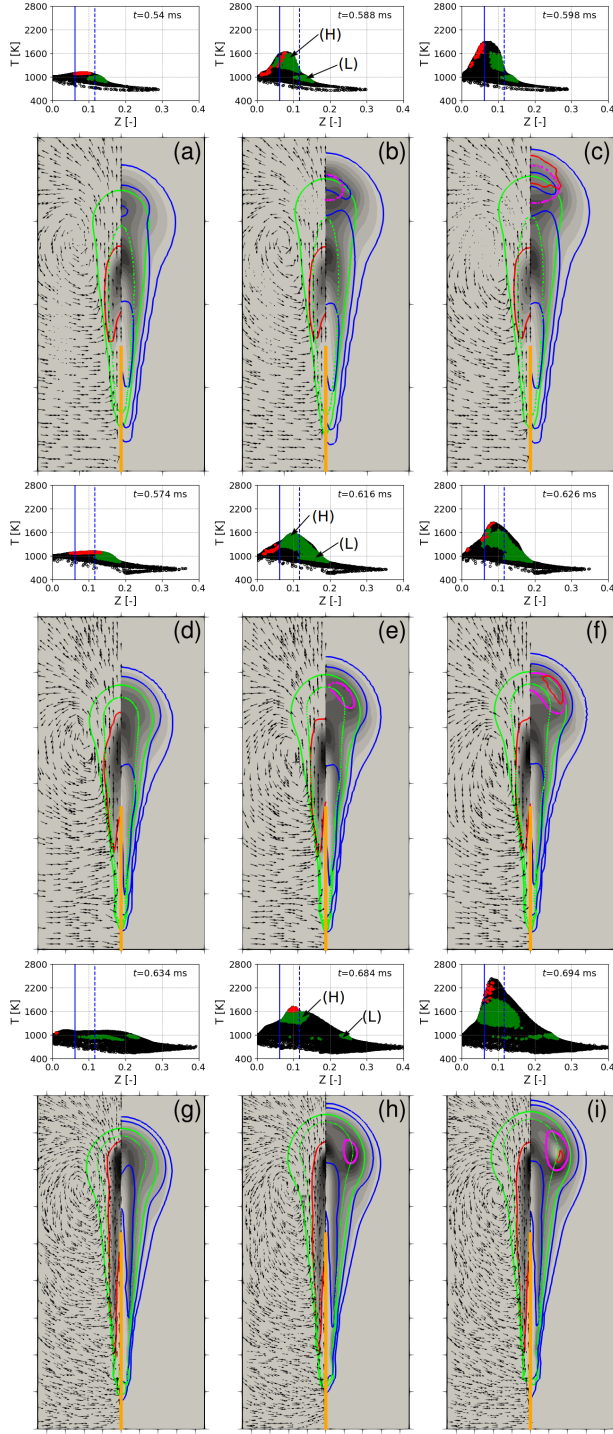
Figure 4: Velocity vectors and contours of combustion products in the 14.8 kg/m^3 case for D_{noz} of (a–c) 100 μm, (d–f) 180 μm, and (g–i) 363 μm. Above them are their corresponding scatter plot of temperature-mixture fraction (T-Z). Left, middle and right columns represent the low-temperature ignition stage, onset of high-temperature ignition, and formation of a classical diesel spray flame. Scatter plots: Cells with substantial formation of HO$_2$ and OH are marked wth green and red, respectively. The thresholds are set to 70 % of their respective maximum mass fraction. Stoichiometric and most reactive mixture fractions are represented by solid blue and dashed blue lines, respectively. Contours (a–i): (Left) Ketohyroperoxide contour with velocity vectors (black arrows) and RO$_2$ mass fraction of 0.001 (solid red); and (Right) HO$_2$ contour with isolines of scalar dissipation rates of 1, 10, and 100 (solid blue), OH mass fraction of 1×10^{-4} (solid red), and temperature of 1400 K (magenta). Maximum mass fraction of KET and HO$_2$ are fixed at 0.003 and 0.0006, respectively. Solid green lines indicate the stoichiometric line and the orange line represent the averaged liquid length. Each frame in (a–c) shows 20 × 40 mm, (d–f) shows 30 × 60 mm, and (g–i) shows 45 × 90 mm.
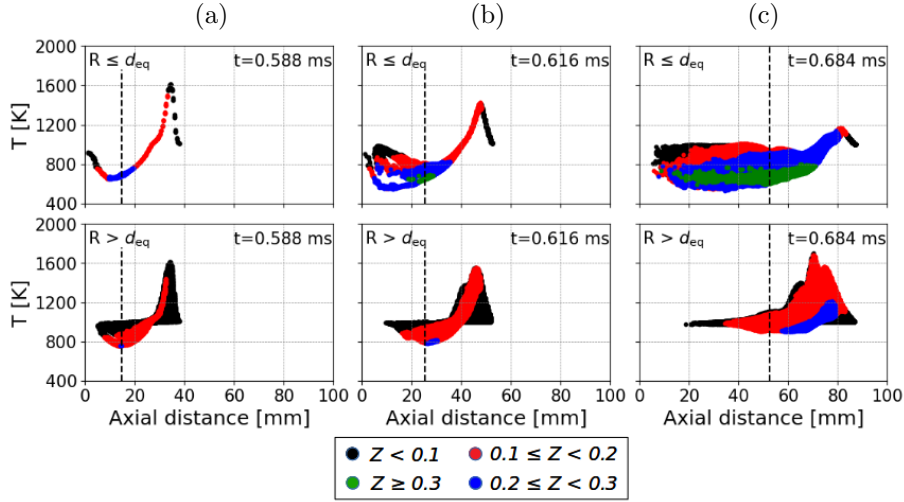
13

Figure 5: Scatter plots of temperature (T) colored by different ranges of mixture fraction (Z) at the onset of high-temperature ignition for D_{noz} of (a) $100\,\mu$m, (b) $180\,\mu$m, and (c) $363\,\mu$m at ρ_{am} of $14.8\,$kg/m^3. Dashed vertical lines represent the liquid penetration length. Top row: spray central region ($R \leqslant d_{\mathrm{eq}}$). Bottom row: spray periphery ($R > d_{\mathrm{eq}}$).

278   to that in the spray periphery (cf. Figures 5). The overly fuel-rich region
279   ($Z > 0.2$), which has a lower temperature, in the spray central region is,
280   hence, expected to be unfavorable for ignition. This observation is supported by
281   findings from the large eddy simulation results in [23] and the two-dimensional
282   direct numerical simulation conducted by Krisman et al. [40]. It is shown that
283   the cool-flame takes a longer time to reach the most fuel-rich mixture [40].
284   Meanwhile, the fuel-rich mixture itself takes a longer time to have a spontaneous
285   ignition due to having a longer low-temperature IDT as shown in the zero-
286   dimensional homogeneous reactor simulation results (see Figure A1 in Appendix
287   A1). This corresponds well to the findings in [41]. These reasons may explain
288   the observation where the high-temperature ignition is more inclined to occur
289   at the spray periphery than at the spray center region as D_{noz} increases.

290   *5.2. Ignition characteristics at $\rho_{\mathrm{am}} = 30.0\,kg/m^3$*

291   At a higher ambient density of $\rho_{\mathrm{am}} = 30.0\,$kg/m^3 (Figure 6), the formation of
292   RO$_2$, KET and HO$_2$ starts earlier for the $100\,\mu$m nozzle case. From Figures 6a,

14

293 HO$_2$ are also formed in the fuel-rich region where local temperature exceeds
294 1100 K. The same phenomenon is observed for the larger D_{noz} cases of 180 and
295 363 μm. However, at this high ρ_{am}, HO$_2$ does not form at two distinct regions
296 during the onset of high-temperature ignition as that observed at a lower ρ_{am}
297 of 14.8 kg/m^3. Instead, HO$_2$ is shown to form across a wide range of Z and T,
298 as shown in the T-Z diagrams of Figures 6b, 6e, and 6h. The high-temperature
299 ignitions across different D_{noz} occur at the fuel-rich side. This observation
300 is similar to that observed in the 14.8 kg/m^3 case discussed above, although
301 the transition period from low- to high-temperature ignition is now shorter.
302 This is expected as a shorter transition is also observed in the homogeneous
303 reactor calculation (see Figure A1 in Appendix A1) as well as in [25]. With a
304 shorter transition time, the ignition location are now nearer to the liquid jet
305 which is highly fuel-rich at the inner core. This, consequently, results in the
306 ignition location to occur at the spray periphery which is relatively less fuel-
307 rich. Figure 7 shows the scatter plots of T, colored by different ranges of Z,
308 along the spray axis for both the central and peripheral region of different D_{noz}
309 at ρ_{am} of 30.0 kg/m^3. In all three D_{noz} cases, the high-temperature ignitions
310 occur at $R > d_{\mathrm{eq}}$ as well as being closer to the liquid jet. As shown in the top
311 row of Figure 7, the inner cores of the spray are more fuel-rich ($Z > 0.2$) and
312 have low temperature, which makes them unfavorable for ignition to occur. The
313 above explanation agrees with the experimental results presented by Higgins et
314 al. [19] for $D_{\mathrm{noz}} = 246\,\mu$m.

315 *5.3. Ignition characteristics at $\rho_{\mathrm{am}} = 58.5\,kg/m^3$*

316   The phenomena are akin to those observed at 30.0 kg/m^3. From Figure 8, it
317 is also obvious that the ignition locations for all three D_{am} are all at the spray
318 periphery. This can again be explained by analyzing the T and Z along the
319 spray axis. Figure 9 shows the scatter plots of T, colored by different ranges of
320 Z, along the spray axis for both the central and peripheral region of different
321 D_{noz} at $\rho_{\mathrm{am}} = 58.5$ kg/m^3. From the figure, the inner core is shown to be too
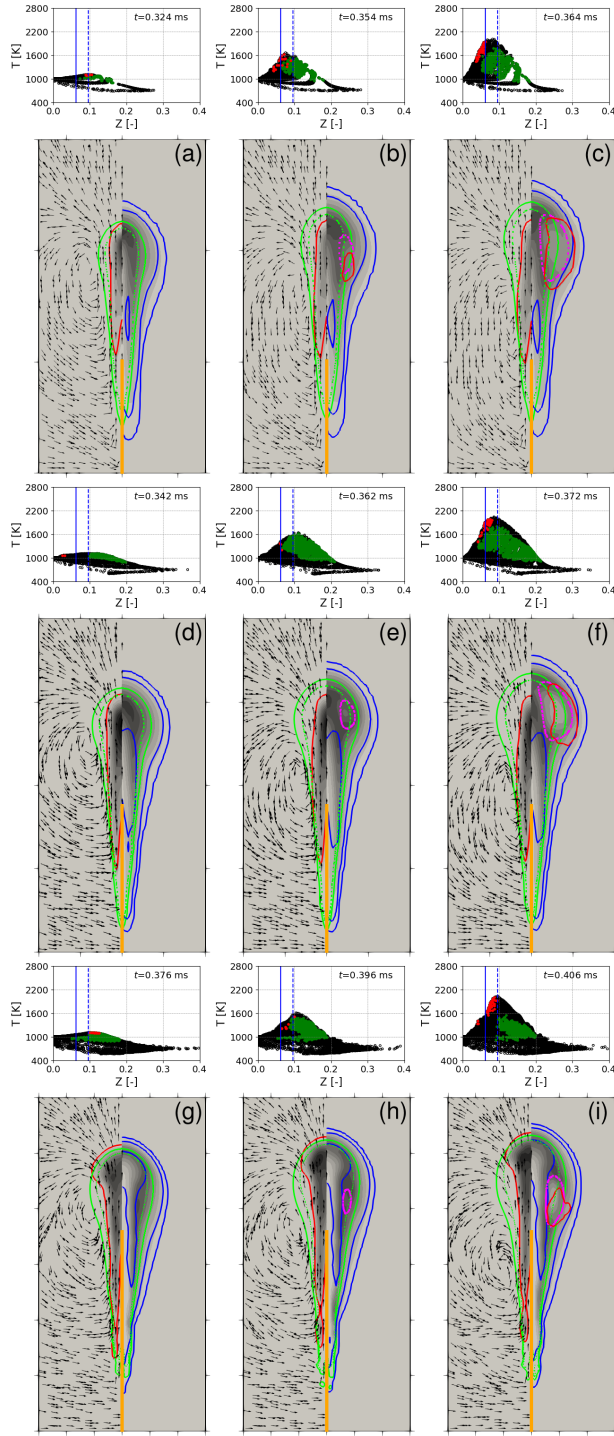322 fuel-rich to be conducive for ignition, thus ignition occurs at the sides instead.

15

Figure 6: Velocity vectors and contours of combustion products in the 30.0 kg/m³ case for D_{noz} of (a-c) 100 μm, (d-f) 180 μm, and (g-i) 363 μm at different times. Above them are their corresponding scatter plot of temperature-mixture fraction (T-Z). Descriptions can be found in the caption of Figure 4. Each frame in (a-c) shows 15 × 30 mm, (d-f) shows 20 × 40 mm, and (g-i) shows 30 × 60 mm.
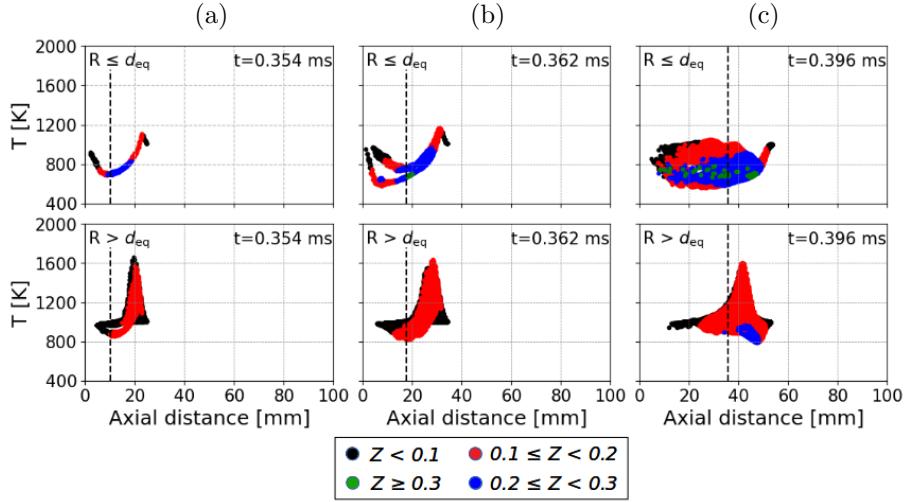
Figure 7: Scatter plots of temperature (T) colored by different ranges of mixture fraction (Z) at the onset of high-temperature ignition for D_{noz} of (a) $100\,\mu m$, (b) $180\,\mu m$, and (c) $363\,\mu m$ at ρ_{am} of $30.0\,kg/m^3$. Dashed vertical lines represent the liquid penetration length. Top row: spray central region ($R \leqslant d_{eq}$). Bottom row: spray periphery ($R > d_{eq}$).

Furthermore, it is also illustrated in Figure 9 that the ignition location is closer to the liquid jet at this high ρ_{am} condition than in the low ρ_{am} cases. This is expected as the ambient density increases even further, the transition from low- to high-temperature ignition shortens considerably. This consequently leads to the ignition to occur much closer to the liquid jet.

In this high ρ_{am} case of $58.5\,kg/m^3$, the high-temperature ignitions for both $100\,\mu m$ and $180\,\mu m$ cases occur at fuel-lean region. The observation for the $180\,\mu m$ case agrees with a similar work from literature [25] which simulated the exact same setup by using a smaller n-heptane mechanism. However, this is not the case when D_{noz} increase to $363\,\mu m$ which shows the ignition to occur at the fuel-rich region. This difference is likely attributed to the longer IDT for the $363\,\mu m$, $58.5\,kg/m^3$ case, which causes significant amount of HO_2 to form in the fuel-rich region and consequently resulting in the fuel-rich mixture igniting. Another reason can be related to the overly fuel-rich mixture at the spray core as shown in Figure 9c. Evaporative cooling is more significant in the large nozzle

17

case as more liquid fuel is injected and longer LPL is observed. The stronger evaporative cooling of the liquid fuel in the large nozzle case prevents ignition to occur at $Z < 0.1$ as observed in the 100 and $180\,\mu$m cases (cf. Figures 9a and 9b). Only until the cool-flame has spread to a relatively fuel-rich region that leads to high-temperature ignition. This also leads to a longer IDT observed for the $363\,\mu$m nozzle case.

5.4. Effects of D_{noz} and ρ_{am} on ignition delay time

As shown previously (Figure 3) the IDT increases as D_{noz} increases. This can be attributed to the different values of local scalar dissipation rate (χ) for different D_{noz} and at varying ρ_{am}, as shown in Figure 10. Figure 10 shows the scatter plot of OH and χ for varying D_{noz} at ρ_{am} of (a) $14.8\,\mathrm{kg/m^3}$, (b) $30.0\,\mathrm{kg/m^3}$, and (c) $58.5\,\mathrm{kg/m^3}$ during the onset of high-temperature ignition. From the figure, the χ for the $363\,\mu$m nozzle case is consistently larger than the $100\,\mu$m case by at least a factor of 3. A high χ leads to longer IDT [41], hence explaining the longer IDT obtained as D_{noz} increases.

It is also depicted in Figure 3 that IDT becomes shorter as ρ_{am} increases. As aforementioned in Section 5.2, the shorter IDT is likely attributed to the shorter chemical time scale when the ambient density increases. The findings are supported by the homogeneous reactor results (see Figure A1 in Appendix A1) and the results in [25], which show shorter IDT as ρ_{am} increases from 14.8 to $58.5\,\mathrm{kg/m^3}$.

6. Conclusion

The present work performed an Unsteady Reynolds Averaged Navier-Stokes simulations coupled with Eulerian Stochastic Field method to study the effects of nozzle diameter (D_{noz}) and ambient density (ρ_{am}) on ignition characteristics in Diesel #2 spray flames. The numerical model is able to capture the ignition processes for different D_{noz} of 100, 180, and $363\,\mu$m at ρ_{am} of 14.8, 30.0, and $58.5\,\mathrm{kg/m^3}$. Comparisons to measurements show that the ignition delay times are well predicted.

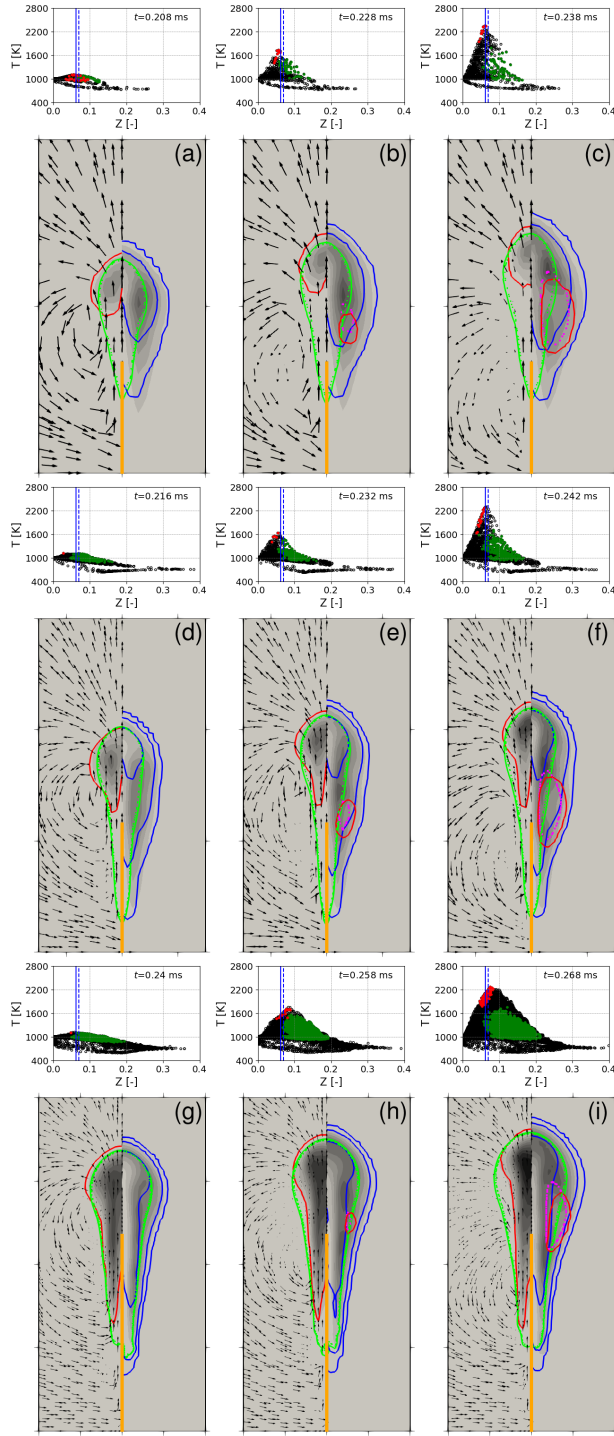Figure 8: Velocity vectors and contours of combustion products in the 58.5 kg/m³ case for D_{noz} of (a-c) 100 μm, (d-f) 180 μm, and (g-i) 363 μm at different times. Above them are their corresponding scatter plot of temperature-mixture fraction (T-Z). Descriptions can be found in the caption of Figure 4. Each frame in (a-c) shows 10 × 20 mm, (d-f) shows 15 × 30 mm, and (g-i) shows 20 × 40 mm.
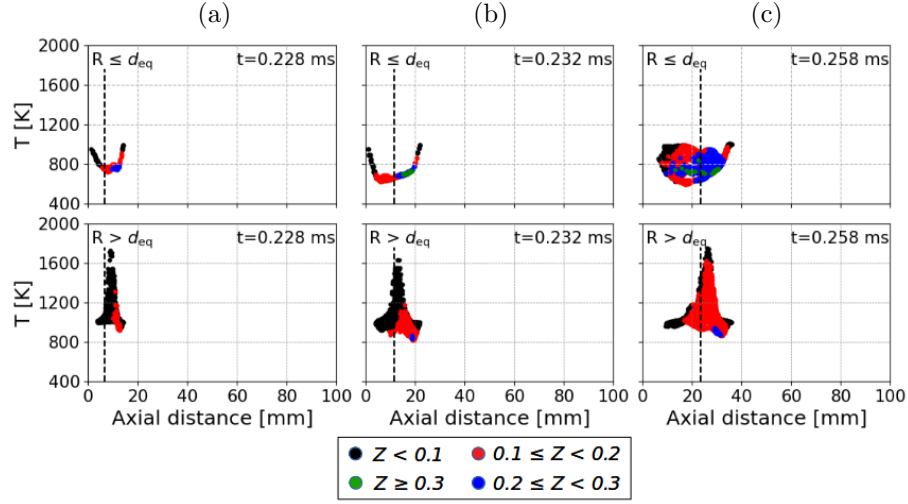
Figure 9: Scatter plots of temperature (T) colored by different ranges of mixture fraction (Z) at the onset of high-temperature ignition for D_{noz} of (a) $100\,\mu$m, (b) $180\,\mu$m, and (c) $363\,\mu$m at ρ_{am} of $58.5\,\mathrm{kg/m^3}$. Dashed vertical lines represent the liquid penetration length. Top row: spray central region ($R \leqslant d_{\mathrm{eq}}$). Bottom row: spray periphery ($R > d_{\mathrm{eq}}$).
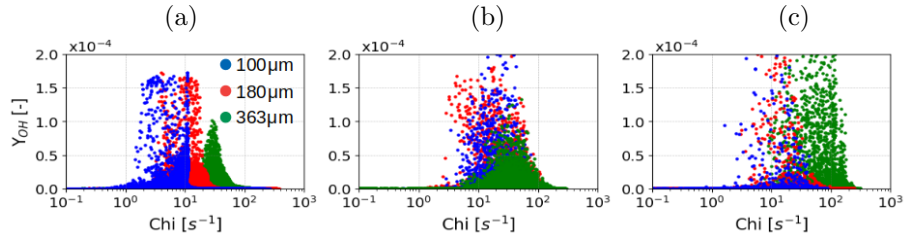

Figure 10: Scatter plots of mass fraction of OH and scalar dissipation rate (OH-χ) at the onset of high-temperature ignition for different ρ_{am} of (a) $14.8\,\mathrm{kg/m^3}$, (b) $30.0\,\mathrm{kg/m^3}$, and (c) $58.5\,\mathrm{kg/m^3}$, as well as D_{noz} of 100, 180, and $363\,\mu$m.

20

For the low density case $(14.8\,\mathrm{kg/m^3})$, the high-temperature ignition location is predicted to shift from the spray tip towards the spray periphery as D_noz increases. The current result suggests that the mixture at the spray central region (including the spray tip) are getting more fuel-rich $(Z > 0.2)$ as D_noz increases. This leads to the spray central region being unfavorable for ignition due to being overly fuel-rich and having lower temperature. Instead, the ignition occurs at the periphery of the spray where $Z \leqslant 0.2$. As ρ_am increases to 30.0 and $58.5\,\mathrm{kg/m^3}$, the ignition locations for all D_noz cases are occurring at the spray periphery. This is because of the shorter ignition timing and the overly fuel-rich spray central region.

The numerical results show that the mixture fraction of the first igniting mixture during the high-temperature ignition across different D_noz are at the fuel-rich region at ρ_am of 14.8 and $30.0\,\mathrm{kg/m^3}$. However, this is not the case when ρ_am increases to $58.5\,\mathrm{kg/m^3}$. The igniting mixture still occurs at the fuel-rich region for the $363\,\mu\mathrm{m}$ nozzle case, but it occurs at the fuel-lean side for the D_noz cases of 100 and $180\,\mu\mathrm{m}$. This can be attributed to the relatively longer ignition delay time in the $363\,\mu\mathrm{m}$ nozzle case. The longer ignition delay time as D_noz increases can be related to the higher local scalar dissipation rate observed in the large nozzle case.

Acknowledgements

References

[1] Engine combustion network.
    URL https://ecn.sandia.gov/

[2] L. M. Pickett, D. L. Siebers, Soot in diesel fuel jets: effects of ambient temperature, ambient density, and injection pressure, Combustion and Flame 138 (1-2) (2004) 114–135.

[3] L. M. Pickett, D. L. Siebers, Orifice diameter effects on diesel fuel jet flame structure, Journal of Engineering for Gas Turbines and Power 127 (1) (2005) 187–196.

[4] L. M. Pickett, D. L. Siebers, Soot formation in diesel fuel jets near the lift-off length, International Journal of Engine Research 7 (2) (2006) 103–130.

[5] A. Krisman, E. R. Hawkes, M. Talei, A. Bhagatwala, J. H. Chen, A direct numerical simulation of cool-flame affected autoignition in diesel engine-relevant conditions, Proceedings of the Combustion Institute 36 (3) (2017) 3567–3575.

[6] R. N. Dahms, G. A. Paczko, S. A. Skeen, L. M. Pickett, Understanding the ignition mechanism of high-pressure spray flames, Proceedings of the Combustion Institute 36 (2) (2017) 2615–2623.

[7] P. Kundu, M. M. Ameen, S. Som, Importance of turbulence-chemistry interactions at low temperature engine conditions, Combustion and Flame 183 (2017) 283–298.

[8] Y. Pei, E. R. Hawkes, M. Bolla, S. Kook, G. M. Goldin, Y. Yang, S. B. Pope, S. Som, An analysis of the structure of an n-dodecane spray flame using TPDF modelling, Combustion and Flame 168 (2016) 420–435.

[9] F. Westlye, Experimental Study of Liquid Fuel Spray Combustion, Technical University of Denmark (DTU), 2016.

[10] J. V. Pastor, J. M. Garcia-Oliver, A. Garcia, A. M. López, An experimental investigation on spray mixing and combustion characteristics for spray C/D nozzles in a constant pressure vessel, SAE Technical Paper, 2018-01-1783.

[11] N. Kyriakides, C. Chryssakis, L. Kaiktsis, Influence of heavy fuel properties on spray atomization for marine diesel engine applications, SAE Technical Paper, 2009-01-1858.

[12] P. Kilpinen, Optimization of a simplified sub-model for NO emission prediction by CFD in large 4-stroke marine diesel engines, Fuel Processing Technology 91 (2) (2010) 218–228.

[13] R. Ishibashi, D. Tsuru, An optical investigation of combustion process of a direct high-pressure injection of natural gas, Journal of Marine Science and Technology 22 (3) (2017) 447–458.

[14] A. Schmid, B. von Rotz, R. Bombach, G. Weisser, K. Herrmann, K. Boulouchos, Ignition behaviour of marine diesel sprays, in: COMODIA Conference, Fukuoka, Japan, 2012.

[15] M. Bolla, A. Srna, Y. M. Wright, B. Von Rotz, K. Herrmann, K. Boulouchos, Influence of injector diameter (0.2-1.2 mm range) on diesel spray combustion: measurements and cfd simulations, SAE Technical Paper, 2014-01-1419.

[16] D. Siebers, Scaling liquid-phase fuel penetration in diesel sprays based on mixing-limited vaporization, SAE Transactions (1999) 703–728.

[17] J. Naber, D. Siebers, Effects of gas density and vaporization on penetration and dispersion of diesel sprays, SAE Transactions (1996) 82–111.

[18] D. Siebers, B. Higgins, Flame lift-off on direct-injection diesel sprays under quiescent conditions, SAE Transactions, 2001-01-0530 (2001) 400–421.

[19] B. Higgins, D. Siebers, A. Aradi, Diesel-spray ignition and premixed-burn behavior, SAE Transactions, 2000-01-0940 (2000) 961–984.

[20] K. Cung, D. C. Bitsis, T. Briggs, V. Kalaskar, Z. Abidin, B. Shah, J. Miwa, Effect of micro-hole nozzle on diesel spray and combustion, SAE Technical Paper, 2018-01-0301.

23

[21] P. Senecal, E. Pomraning, K. Richards, T. Briggs, C. Choi, R. McDavid, M. Patterson, Multi-dimensional modeling of direct-injection diesel spray liquid length and flame lift-off length using CFD and parallel detailed chemistry, SAE Transactions (2003) 1331–1351.

[22] J. M. Desantes, J. M. García-Oliver, R. Novella, L. Pachano, A numerical study of the effect of nozzle diameter on diesel combustion ignition and flame stabilization, International Journal of Engine Research.

[23] J. C. Ong, K. M. Pang, X.-S. Bai, J. H. Walther, Large-eddy simulation of n-dodecane spray flame: Effects of nozzle diameter on autoignition at varying ambient temperatures, Proceedings of the Combustion Institute (2020) Article in press.

[24] K. M. Pang, M. Jangi, X.-S. Bai, J. Schramm, J. H. Walther, Effects of nozzle diameter on diesel spray flames: A numerical study using an eulerian stochastic field method, Energy Procedia 142 (2017) 1028–1033.

[25] K. M. Pang, M. Jangi, X.-S. Bai, J. Schramm, J. H. Walther, P. Glarborg, Effects of ambient pressure on ignition and flame characteristics in diesel spray combustion, Fuel 237 (2019) 676–685.

[26] K. M. Pang, M. Jangi, X.-S. Bai, J. Schramm, Evaluation and optimisation of phenomenological multi-step soot model for spray combustion under diesel engine-like operating conditions, Combustion Theory and Modelling 19 (3) (2015) 279–308.

[27] T.-H. Shih, W. W. Liou, A. Shabbir, Z. Yang, J. Zhu, A new k-epsilon eddy viscosity model for high reynolds number turbulent flows, Computers & Fluids 24 (3) (1995) 227–238.

[28] R. D. Reitz, R. Diwakar, Structure of high-pressure fuel sprays, SAE Transactions, 870598 (1987) 492–509.

[29] R. Lin, L. L. Tavlarides, Thermophysical properties needed for the development of the supercritical diesel combustion technology: Evaluation

24

of diesel fuel surrogate models, The Journal of Supercritical Fluids 71 (2012) 136–146.

[30] L. Valino, A field Monte Carlo formulation for calculating the probability density function of a single scalar in a turbulent flow, Flow, Turbulence and Combustion 60 (2) (1998) 157–172.

[31] M. Jangi, T. Lucchini, C. Gong, X.-S. Bai, Effects of fuel cetane number on the structure of diesel spray combustion: An accelerated Eulerian stochastic fields method, Combustion Theory and Modelling 19 (5) (2015) 549–567.

[32] K. M. Pang, M. Jangi, X.-S. Bai, J. Schramm, J. H. Walther, Modelling of diesel spray flames under engine-like conditions using an accelerated eulerian stochastic field method, Combustion and Flame 193 (2018) 363–383.

[33] M. Jangi, R. Yu, X.-S. Bai, Development of chemistry coordinate mapping approach for turbulent partially premixed combustion, Flow, Turbulence and Combustion 90 (2) (2013) 285–299.

[34] T. Lu, C. K. Law, Strategies for mechanism reduction for large hydrocarbons: n-heptane, Combustion and Flame 154 (1-2) (2008) 153–163.

[35] S. Liu, J. C. Hewson, J. H. Chen, H. Pitsch, Effects of strain rate on high-pressure nonpremixed n-heptane autoignition in counterflow, Combustion and Flame 137 (3) (2004) 320–339.

[36] S. Som, P. K. Senecal, E. Pomraning, Comparison of RANS and LES turbulence models against constant volume diesel experiments, in: ILASS Americas, 24th Annual Conference on Liquid Atomization and Spray Systems, San Antonio, TX, 2012.

[37] J. Manin, M. Bardi, L. Pickett, R. Payri, Boundary condition and fuel composition effects on injection processes of high-pressure sprays at the

25

502 microscopic level, International Journal of Multiphase Flow 83 (2016) 267–
503 278.

[38] Y. Pei, S. Som, E. Pomraning, P. K. Senecal, S. A. Skeen, J. Manin, L. M.
Pickett, Large eddy simulation of a reacting spray flame with multiple
realizations under compression ignition engine conditions, Combustion and
Flame 162 (12) (2015) 4442–4455.

[39] A. Irannejad, A. Banaeizadeh, F. Jaberi, Large eddy simulation of
turbulent spray combustion, Combustion and Flame 162 (2) (2015) 431–
450.

[40] A. Krisman, E. R. Hawkes, J. H. Chen, A parametric study of ignition
dynamics at ECN Spray A thermochemical conditions using 2D DNS,
Proceedings of the Combustion Institute 37 (4) (2019) 4787–4795.

[41] G. Borghesi, A. Krisman, T. Lu, J. H. Chen, Direct numerical simulation of
a temporally evolving air/n-dodecane jet at low-temperature diesel-relevant
conditions, Combustion and Flame 195 (2018) 183–202.

Appendix

A1: Autoignition in 0-D homogeneous reactor

The autoignition characteristics of Lu68 mechanism is first evaluated by

performing a zero-dimensional (0-D) homogeneous reactor calculations at three

different initial ambient density (ρ_{am}) of 14.8, 30.0, and 58.5 kg/m^3 and three

different nozzle diameter (D_{noz}) of 100, 180, and 363 μm using the Ansys CHEMKIN-

PRO software. The high-temperature ignition delay time (IDT$_{HT}$) here is

defined as the time where the mixture temperature increase to 400 K above the

initial temperature ($T_{t=0}$). Mass fraction of heptyl radical, C$_7$H$_{15}$O$_2$ (RO$_2$ is

henceforth used for brevity) is used as an indicator for the low-temperature

ignition (LTI) activity. Therefore, the low-temperature ignition delay time

(IDT$_{LT}$) is defined here as the time where the maximum mass fraction of RO$_2$

is attained.

A quadratic correlation (Equation 1) between temperature and mixture

fraction can be obtained by postprocessing the 3D-CFD reacting case results

prior to the onset of LTI.

$$T_{t=0} = T_{am} + 1120Z^2 - 1370Z \tag{1}$$

In Equation 1, Z denotes the mixture fraction while T_{am} denotes the initial

ambient temperature in the combustion chamber which is set as 1000 K. This

quadratic correlation corresponds to the mixing of vapor fuel and hot ambient

air. Therefore, it is also known as the spray mixing line. Equation 1 is

constructed for $0 \leqslant Z \leqslant 0.4$ and the equation is found to be applicable for

all three ρ_{am} and three D_{noz} cases (not shown). The most reactive mixture

fraction (Z_{mr}) is defined as the mixture which has the shortest IDT$_{HT}$, and the

associated IDT is known as most reactive IDT (IDT$_{mr}$).

From Figure A1a, Z_{mr} is shown to decrease and move towards the stoichiometric

mixture fraction (Z_{st}) with increasing ρ_{am}. The Z_{mr} are recorded to be 0.117,

0.096, and 0.070 for the 14.8, 30.0, and 58.5 kg/m^3 cases, respectively. The

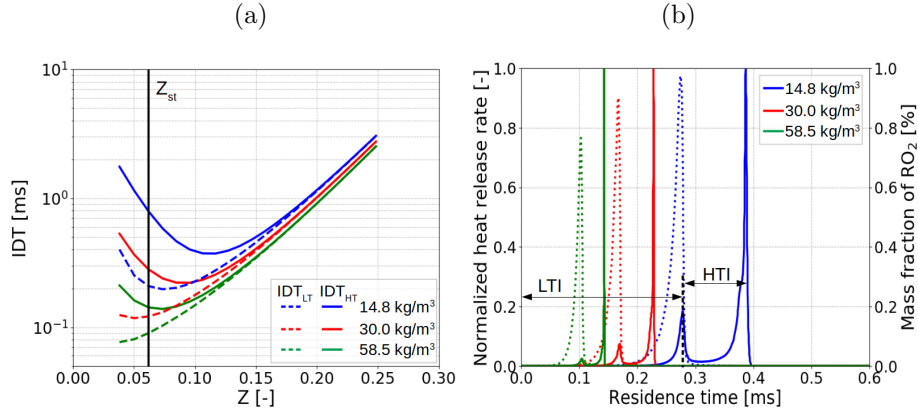corresponding $T_{t=0}$ are 855, 879, 905 K. As the same correlation (Eq. 1) is

Figure A1: (a) Low-temperature (IDT$_{\text{LT}}$) and high-temperature ignition delay times (IDT$_{\text{LT}}$) of homogeneous mixtures for various initial mixture fractions (Z) and temperatures (T) at ρ_{am} of 14.8, 30.0, and 58.5 kg/m^3. Solid vertical black line represents stoichiometric mixture fraction (Z_{st}) of 0.062. (b) Temporal evolution of normalized heat release rate (HRR) of Z_{mr} computed in the 0-D homogeneous reactor model at ρ_{am} of 14.8, 30.0, and 58.5 kg/m^3. Solid lines represent the normalized HRR. Dotted lines represent mass fraction of RO$_2$.

545 applicable across different D_{noz} for a given ρ_{am}, the Z_{mr} obtained from Figure A1a

546 is applicable for all three D_{noz}. This also implies that D_{noz} has no significant

547 effect on Z_{mr} in the present study. In addition to this, Figure A1a also shows

548 that both IDT$_{\text{LT}}$ and IDT$_{\text{HT}}$ become shorter as ρ_{am} increases. Furthermore,

549 longer IDTs are obtained as the mixture becomes richer (Z increases) and has

550 a lower temperature ($T_{t=0}$ decreases). It is also worth mentioning that the

551 dwell period between LTI and high-temperature ignition (HTI) decreases as the

552 mixture becomes richer (cf. Figure A1a). This is similarly shown for n-dodecane

553 fuel in [41].

554   Figure A1b depicts the simulated heat releases rate (HRR) at the most

555 reactive states for each ρ_{am} case. The temporal evolution of RO$_2$ of these cases

556 are also provided in the figure. It is evidently shown in Figure A1b that the LTI

557 and HTI stages coincide with the peak of RO$_2$ and HRR. Moreover, the HTI

558 stage is also shown to occur after RO$_2$ is consumed.